Nanoporous CuCo2O4 nanosheets as a highly efficient bifunctional electrode for supercapacitors and water oxidation catalysis

Sambhaji M. Pawar,[a] Bharati S. Pawar,[a] Pravin T. Babar,[b] Abu Talha Aqueel Ahmed,[a] Harish S. Chavan,[a] Yongcheol Jo,[a] Sangeun Cho,[a] Jongmin Kim,[a] Bo Hou,[c] Akbar I. Inamdar,[a] SeungNam Cha,[c] Jin Hyeok Kim,[b] Hyungsang Kim [a] and Hyunsik Im *[a]*

[a] Division of Physics and Semiconductor Science, Dongguk University, Seoul 04620, South Korea

[b] Optoelectronic Convergence Research Center, Department of Materials Science and Engineering, Chonnam National University, Gwangju 500-757, South Korea

[c] Department of Engineering Science, University of Oxford, Parks Road, OX1 3PJ, UK

ABSTRACT

Ultrathin nanoporous $CuCo_2O_4$ nanosheets can be synthesized on nickel foam (NF) via an electrodeposition method followed by air annealing treatment. The electrochemical energy storage and oxygen evolution reaction (OER) properties are studied in aqueous 1M KOH solution. The $CuCo_2O_4$ nanosheet electrode exhibits a high specific capacitance of 760 F/g at 1 A/g with a capacity retention of ~ 85% after 5000 cycles and 1473 F/g at 1 A/g in 3M KOH solution. The $CuCo_2O_4$ nanosheet electrode works as a highly efficient OER electrocatalyst, demonstrating an overpotential of 260 mV at 20 mA/cm^2 with a Tafel slope of ~ 64 mV/dec., which is the lowest among other copper-cobalt based transition metal oxide catalysts. The catalyst is very stable at > 20 mA/cm^2 for more than 25 h. The superior electrochemical performance of the $CuCo_2O_4$ nanosheets is due to the synergetic effect of the direct growth of 2D nanosheet structure and a large electrochemically active surface area associated with nanopores on the $CuCo_2O_4$ nanosheet surface.

Keywords: $CuCo_2O_4$ nanosheets, electrodeposition, supercapacitor, electrocatalyst, oxygen evolution reaction.

E-mail: spawar81@gmail.com (S.M. Pawar), hyunsik7@dongguk.edu (Hyunsik Im)

1. Introduction

The development of efficient, cheap and clean energy storage/conversion devices has become a challenging issue due to a continuous increasing energy consumption, the rapid depletion of fossil fuels and an increase in the environmental pollution.[1,2] Among various energy storage and conversion devices, supercapacitors (SCs) and hydrogen generation based on water electrocatalysis are considered to be promising technologies that can help to solve the pressing issues. A key advantage of these technologies is the cost-effective fabrication of efficient electrode materials using inexpensive and earth-abundant elements. Recently, transition metal oxides (TMOs) such as RuO_2,[3,4] NiO,[5,6] CuO,[7,8] Co_3O_4,[9] Fe_2O_3,[10,11] MnO_2,[12,13] and MoO_2,[14,15] have been intensively investigated as electrode materials, because they possess multiple oxidation states that can enhance electrochemical redox reactions.[16] Among the various TMOs, spinel cobaltites (MCo_2O_4, M = Ni, Cu, Zn, Mn etc.) have enhanced electrochemical activities compared with single component metallic oxides (MO_x).[16-17] The Co_3O_4 adopts a normal spinel structure in which the Co^{2+} and Co^{3+} ions occupy the tetrahedral and octahedral interstices, respectively.[18] According to the site preference theory ,[19] the Co cation is partially substituted by a transition metal (i.e., Cu, Ni and Mn) cation, which occupies the octahedral sites, while Co occupies both the tetrahedral and octahedral sites and forms an inverse spinel structure.[20-23] This structure contains 3D networks of the interconnected interstitial space, where the four apexes of the tetrahedron are shared with the octahedron. Hence, it can provide efficient channels for ion diffusion contribution toward charge carriers (electrons or holes) that hop into the tetrahedral and octahedral sites for high electrical conduction.[24]

Recently, ternary metal oxide materials based on copper cobalt (CuCo) have attracted great interest because of their earth-abundance, high theoretical capacity, outstanding redox

capability, good anticorrosion performance in alkaline environment, and reasonably good catalytic properties; furthermore, their electrical conductivity and electrochemical activity are much higher than those of single component copper oxides and cobalt oxides due to their multiple oxidation states.[16,25] In order to enhance the electrochemical activity of $CuCo_2O_4$, much effort has been devoted to exploring facile synthesis, morphology engineering and chemical/structural optimization.[16,17,25-39] Two-dimensional (2D) ultrathin nanosheets are more favorable for energy conversion and storage devices because their unique morphologies can provide easy diffusion paths for ions and electrons, large electrochemically active sites at the electrode-electrolyte interface, high electrical conductivity, and improved structural stability.[40] Although some research groups have reported the synthesis of $CuCo_2O_4$ with various nanomorphologies as supercapacitor electrodes,[16,26,27,29-39] its capability for water splitting catalysis is rarely investigated.[25,28,31,41-44] A general development strategy for oxygen evolution reaction (OER) catalysts is to search for a facile route to synthesize cheap, efficient catalytic materials with optimized chemical compositions and morphologies. However, nanosheets deposited on planar substrates have limited available active sites because only few outermost layers are in contact with electrolytes. Furthermore, the accumulation of gas bubbles, which are generated during the OER, can decrease the electrochemical activity.[45] To overcome this problem, the surface area of the substrate should be a three-dimensional (3D) open-pore structure that provides efficient charge transport pathways for electrons and ions during the redox reaction and promotes the evolution and release of gas bubbles from the catalyst surface during the electrolysis process.[46]

In this study, we report the direct synthesis of $CuCo_2O_4$ nanosheets with a unique nanoporous surface morphology on a nickel foam (NF) substrate via an electrodeposition method.

We demonstrated that the nanosheet film works as a highly-efficient bifunctional electrode for both electrochemical energy storage and water splitting catalysis in an alkaline 1M KOH solution. The $CuCo_2O_4$ nanosheet electrode exhibits a specific capacitance of 760 F/g at 1 A/g and a long-term capacity retention of 85% after 5000 cycles. It also shows a superior electrocatalytic activity for water oxidation with a low overpotential of 260 mV at 20 mA/cm^2. **Figure 1** shows a comparative representation of electrochemical performances i.e. supercapacitor and oxygen evolution reaction (OER) properties of $CuCo_2O_4$ based materials including our own results (see also Table S2 and S3 in the Supporting Information).

2. Experimental

Materials

A $CuCo_2O_4$ nanosheet film was synthesized on a NF substrate via an electrodeposition method. An aqueous electrolytic bath containing 10 mM cobalt nitrate ($Co(NO_3)_2$) and 2.5 mM copper nitrate ($Cu(NO)_3)_2$) was prepared at room temperature. The electrodeposition was carried out in a three-electrode cell where a Pt wire was used as the counter electrode, while the saturated calomel electrode (SCE) and an NF substrate with an area of 1×1 cm^2 served as the reference electrode and the working electrode, respectively. Analytical reagent grade chemicals were used for precursor solution preparation (supplied by Sigma-Aldrich). Prior to the electrodeposition, the NF substrate was first cleaned with a 3 M HCl solution using ultra-sonication for 10 min to remove the nickel oxide layer. The NF substrate was first washed with acetone, ethanol and distilled (DI) water for 10 min and then it was dried at 60 °C for 24 h. The copper-cobalt hydroxide precursor film was deposited at −1.0 V (vs. SCE) in the potentiostatic mode (VERSA-STAT3, Princeton Applied Research) for 300 s. Subsequently, the deposited film

was rinsed with DI water and dried at room temperature. For comparison, a cobalt hydroxide film was fabricated using the $Co(NO_3)_2$ precursor solution at the same synthesis conditions. Both the films were annealed in air atmosphere at 400 ^{0}C with a ramping rate of 2 ^{0}C/min. for 2 h.

The structural and chemical properties of the films were studied using high resolution X-ray diffraction (XRD) with Ni-filtered CuKα radiation [kα= 1.54056 Å] (X'pert PRO, Philips, Eindhoven, Netherlands) and X-ray photoelectron spectroscopy (XPS, VG Multilab 2000, Thermo VG Scientific, UK) with a monochromatic Mg-Kα (1253.6 eV) radiation source. The surface morphology, chemical composition, and crystallinity of the samples were examined using a field emission scanning electron microscopy (FE-SEM, Model: JSM-6701F, JEOL, Japan), energy-dispersive X-ray spectroscopy (EDS), transmission electron microscopy (TEM, JEOL 2010) and selected area electron diffraction (SAED).

Electrochemical measurements:

The electrochemical properties of the electrode films were studied in an aqueous 1 M KOH solution using cyclic voltammetry (CV), galvanostatic charge/discharge (GCD) and electrochemical impedance spectroscopy (EIS) analyses. The weight of deposited film was approximately 0.80 mg. The CV analysis was performed between 0 and 0.5 V (vs. SCE) at scan rates ranging from 5 to 100 mV/s. The GCD test was conducted in a stable potential window between 0 and 0.4 V at different current densities ranging from 1 to 10 A/ g. The EIS measurements were carried out at 0 V in the frequency range of 0.1 Hz to 1 MHz with an AC potential amplitude of 10 mV.

The electrocatalytic activity for the oxygen evolution reaction (OER) of these films was investigated in an aqueous 1 M KOH solution. The potential (E) in this study was referenced to a

reversible hydrogen electrode (RHE) according to the Nernst equation in 1 M KOH ($E_{RHE} = E_{SCE} + 0.059\ pH + E^0_{SCE}$), where E^0_{SCE} is the standard potential of the SCE at 25 °C and the overpotential (η) was obtained by the equation: $\eta = E_{RHE} - 1.23$ V. Linear sweep voltammetry (LSV) was carried out by sweeping the potential from 1 to 1.8 V (vs. RHE) at a scan rate of 5 mV/s, and several polarization curves were recorded until the reproducibility of each measurement was obtained. The chronopotentiometry (CP) measurements were performed to evaluate the long-term stability of the films.

3. Results and Discussion

The XRD patterns of the Co_3O_4 and $CuCo_2O_4$ nanosheet films are shown in **Figure 2.** The three strong diffraction peaks marked with "*" are due to the NF substrate. The well-defined diffraction peaks are observed at 31.4, 37.0, 59.6 and 65.7 for the Co_3O_4 nanosheet electrode, and these are indexed to the (220), (311), (511), and (440) planes of the cubic spinel Co_3O_4, respectively [JCPDS#431003]. No other phase peaks are detected, indicating that the as-deposited amorphous $Co(OH)_2$ nanosheets were transformed into Co_3O_4 after heat treatment **(Figure S1)**. The diffraction peaks of the $CuCo_2O_4$ film appear at similar 2θ angles but their intensities are enhanced. However, binary phases, i.e. CuO and Co_3O_4, are observed at a higher concentration of $Cu(NO_3)_2$ with a percentage of 62.4 % and 37.6 %, respectively. **(Figure S2)**. The average crystallite size was estimated using Scherer's formula,[47] and it was ~ 14 nm for the Co_3O_4 nanosheets and ~ 11 nm for the $CuCo_2O_4$ nanosheets. The reduction in the crystalline grain size of the $CuCo_2O_4$ nanosheets may be attributed to crystallographic disorder in the Cu-Co-O mixed oxides.[48]

We further performed elemental and chemical binding-state analyses of the nanosheet films using energy-dispersive X-ray spectroscopy (EDS) elemental mapping (**Table S1** and **Figure S3**) and X-ray photoelectron spectroscopy (XPS) measurements, as shown in **Figure 3** and **Figure S4**. The uniform distribution of the Cu, Co and O elements with the desired composition are observed in both the films. The full XPS survey spectra of the samples show non-oxygenated carbon (C 1s), Co 2p3/2, Co 2p1/2, and oxygen (O) peaks at 284.6 , 779.84 , 794.90 , and 529.37 eV, respectively. Whereas, the Cu 2p3/2 and Cu 2p1/2 peaks are observed at 933.38 and 953.46 eV for the $CuCo_2O_4$ nanosheet sample. The two satellite peaks are observed with a binding energy of 10 eV higher than that of the main peaks. Which confirms the presence of Cu^{2+} in the sample.[25] The high-resolution Co 2p spectra consist of two spin-orbit doublets with a spin-energy separation of ~ 15 eV and two shake-up satellites (indicated as "Sat"), thus confirming the presence of mixed Co^{2+} and Co^{3+} with a spinel structure.[26] The O 1s spectra of the films are resolved into four components O1, O2, O3 and O4 centered at 528.8, 529.4, 530.8 and 531.7 eV, respectively. The O1 component is associated with typical metal-oxygen bonding, O2 and O3 correspond to the absorbed water and hydroxyl groups and O4 is a higher number of surface oxygen vacancies, which can be observed for samples with small particles.[25]

Figure 4(a,d) shows the SEM images of the Co_3O_4 and $CuCo_2O_4$ nanosheet films, respectively. The ultrathin nanosheets are grown vertically on the NF substrate and they are interconnected with a highly open structure. The nanosheet thickness is approximately 5 to 10 nm and microscopic pores are detected on the nanosheet surface. The pore density on the $CuCo_2O_4$ nanosheet is larger, suggesting that it has a large electrochemically active surface area. The formation of the nanoscale pores on the nanosheet surface can be attributed to the gas ejection during thermal transformation from the metal hydroxide to oxide formation.[49] The TEM

images of the single Co_3O_4 and $CuCo_2O_4$ nanosheets in **Figure 4(b,e)** confirm the formation of nanopores on the nanosheet surface. These ultrathin nanosheets with nanopores are beneficial because such a unique morphology creates a large electrochemically active surface area that is favorable for electrochemical energy storage and electrocatalysis applications.[50] The insets show selected area electron diffraction (SAED) patterns with well-defined diffraction spots and diffused rings indexed to the (111), (220) and (311) planes of the spinel Co_3O_4 and $CuCo_2O_4$ structures, suggesting the polycrystalline nature of the nanosheets.[51] The high-resolution TEM (HR-TEM) images of the samples are shown in **Figure 4(c,f)**. The observed lattice fringes show an interplaner spacing of 0.24 and 0.28 nm that corresponding to the (311) and (220) planes of the spinel Co_3O_4 and 0.47 nm for (111) plane of $CuCo_2O_4$, respectively.[52]

The electrochemical supercapacitive performance of the Co_3O_4 and $CuCo_2O_4$ nanosheet electrodes were evaluated using by cyclic voltammetry (CV), galvanostatic charge/discharge (GCD) and electrochemical impedance spectroscopy (EIS) analyses. **Figure 5 (a,b)** shows the measured CV curves at different scan rates. The CV curves consist of a pair of strong redox peaks, indicating a pseudocapacitive behavior arising from the Faradaic reaction of the $Co^{4+} \leftrightarrow Co^{3+}$ and $Cu^{2+} \leftrightarrow Cu^{+}$ transitions associated with OH^- ions in the electrolyte.[16] As the scan rate increases, the anodic and cathodic peaks shift away from each other. This shift is due to an increase in internal resistance as well as a polarization effect at high scan rates, resulting in the loss of the charge storage capability.[26] However, for the Co_3O_4 nanosheet electrode, a very small cathodic peak is observed at 0.2 V, which is associated with the electrochemical transformation of Co^{3+} to Co^{2+}.[53] The observed CV curves during the cathodic and anodic sweeps are asymmetric, indicating the kinetic irreversibility of the redox reactions, and this is presumably due to polarization and ohmic resistance during the Faradaic process.[54] The

electrochemical redox reactions at the electrolyte/electrode interface in alkaline KOH solution can be described as follows:[16, 31,32, 38,55]

$$Co_3O_4 + OH^- + H_2O \leftrightarrow 3CoOOH + e^- \quad (1)$$

$$CuCo_2O_4 + H_2O + e^- \leftrightarrow 2CoOOH + CuOH \quad (2)$$

$$CoOOH + OH^- \leftrightarrow CoO_2 + H_2O + e^- \quad (3)$$

$$CuOH + OH^- \leftrightarrow Cu(OH)_2 + e^- \quad (4)$$

The specific capacitance (Cs) of the electrode can be calculated using the following equation:

$$C = \frac{1}{2mv(V_c - V_a)} \int_{V_a}^{V_c} I(V)dV \quad (5)$$

where ν is the scan rate, ($V_c - V_a$) is the potential range, $I(V)$ denotes the response current, and m is the weight of the electrode film. **Figure 5(c)** shows the calculated Cs of the nanosheet electrodes as a function of scan rate. The specific capacitance decreases with increasing scan rate due to the redox reaction on the electrode surface. [16] The maximum specific capacitance of the $CuCo_2O_4$ nanosheet electrode is 826 F/g at 5 mV/s, which is nearly double that of the Co_3O_4 nanosheet electrode (420 F/g). From the **Figure 5(d)**, it is clearly seen that the bare Ni foam substrate shows a much smaller current compared with that of the Co_3O_4 and $CuCo_2O_4$ nanosheet electrodes on the NF substrate, revealing its negligible contribution to the total capacitance.

The electrochemically active surface area (ECSA) of the nanosheet electrodes was estimated from the linear charging region of the CV curves, as shown in **Figure S5(a,b)**. The non-Faradaic current i_{DL} was determined by the charge accumulation in the linear charging region. The i_{DL} versus v curves of the electrodes measured at 0.1 V are shown in **Figure S5(c)**. The i_{DL} versus v characteristics are given by the following equation:

$$i_{DL} = C_{DL} \cdot v \quad (6)$$

where C_{DL} represents the double-layer capacitance. The ECSA of the Co_3O_4 and $CuCo_2O_4$ nanosheet electrodes can be calculated using the following equation:

$$ECSA = C_{DL} / Ca \quad (7)$$

where Ca represents the specific capacitance of the alkaline solution. The Ca for KOH electrolyte was 0.04 mF/cm^2.[5] The ECSA value was 1313.6 cm^{-2} for Co_3O_4 and 4712.5 cm^{-2} for $CuCo_2O_4$, revealing that the $CuCo_2O_4$ is much more electrochemically active than the Co_3O_4. The observed large capacitance and electrochemically active surface area of $CuCo_2O_4$ suggest that the additional copper element contributes to improvement in the electrical conductivity and the electrochemically active surface area.

The galvanostatic charge-discharge (GCD) measurements of the electrodes were carried out at various current densities in 1M and 3M KOH solutions as shown in **Figure 6 (a,b)**. The nonlinear GCD curves confirm their pseudocapacitive behavior associated with the Faradaic redox reaction. The specific capacitance (*Cs*) can be obtained from the GCD curves using the following equation:

$$Cs = I \times \Delta t / m\Delta V \quad (8)$$

where I and Δt are the response current and the discharge time, respectively and ΔV is the potential change during the discharging process. **Figure 6(c)** shows the specific capacitance as a function of current density. The specific capacitance decreases with an increasing current density due to the redox reaction at the electrolyte/electrode interface. The maximum specific capacitance of the Co_3O_4 and $CuCo_2O_4$ nanosheet electrodes is 865 and 1473 F/g at 1 A/g in a 3M KOH solution, respectively. The specific capacitance of the bare Ni foam substrate is negligible compared with that of the Co_3O_4 and $CuCo_2O_4$ nanosheet electrodes (**Figure 6(d)**).

The performance of the long-term cycling stability of the electrodes is shown in **Figure 7(a)**. The cycling measurements were carried out at a very high current density of 10 A/g. The Co_3O_4 and $CuCo_2O_4$ nanosheet electrodes show an excellent cycling stability with a capacity retention of ~ 83% and ~ 85% respectively. **Figure 7(b)** shows the Nyquist plot of the electrodes before and after 5000 charge/discharge cycles. The EIS spectra show a smoothly increasing curve without a clear semi-circular feature in the high frequency region and a tilted line in the low frequency region. The absence of the semi-circle with a diameter corresponding to the charge transfer resistance (R_{ct}), associated with the redox reaction on the electrode surface, suggests a negligible charge-transfer resistance. The high-frequency intercept of the curve on the real axis shows the series resistance (R_S), which is a combination of the electronic and ionic resistances of the electrochemical system. The extracted R_S values are 0.45 Ω for $CuCo_2O_4$ and 0.56 Ω for Co_3O_4. The slope of the tilted line (often referred to as the Warburg resistance) represents the diffusion of the electrolyte within the electrode. In the low-frequency region, the $CuCo_2O_4$ nanosheet electrode has a steeper line, revealing a more efficient electrolyte and proton diffusion into the $CuCo_2O_4$ nanosheets. These results confirm that the $CuCo_2O_4$ has better conductivity and a larger electrochemically active surface area. After 5000 cycles, the R_S value for both electrodes is increased.

Figure 8(a,b) shows the OER linear sweep voltammetry (LSV) polarization curves at a scan rate of 5 mV/s and the Tafel plot for the Co_3O_4 and $CuCo_2O_4$ electrodes in 1 M KOH solution. The electrodes have an oxidation peak at ~1.45 V that corresponds to the transition from Ni(II) to Ni(III) due to the Ni foam substrate, which is a common phenomenon in electrocatalyst on Ni foam.[56,57] The Co_3O_4 nanosheet electrode has an overpotential of 330 mV at 20 mA/cm^2 with a Tafel slope of ~ 67 mV/dec. whereas the $CuCo_2O_4$ nanosheet electrode

exhibits a considerably lower overpotential of 260 mV with an improved Tafel slope of ~ 64 mV/dec, revealing its more favorable OER electrocatalytic kinetics. However, the bare Ni foam substrate shows a very high overpotential of 430 mV at 20 mA/cm^2. The OER activity of the $CuCo_2O_4$ nanosheets is considerably higher than that of a recently reported copper-cobalt based transition metal oxide electrocatalyst **(Figure 1(b) and Table S3)**. The significantly improved OER electrocatalytic activity of the $CuCo_2O_4$ nanosheets is due to the Cu species in the octahedral sites of the spinel structure that creates active OER sites with a much lower activation potential than that of the Co cation, and the nanosheet morphology with high-density nanopores contribute to increasing the electrochemically active catalytic sites. The long-term electrocatalytic stability of the catalysts was evaluated using chronopotentiometry, as shown in **Figure 8(c)**. The overpotential of the electrodes at 20 mA/cm^2 remains nearly unchanged up to 25 h, confirming an excellent electrocatalytic stability. The comparable LSV curves **(Figure 8(d))** before and after the stability test reveal their outstanding durability for the OER in a highly alkaline solution. The XRD and SEM analyses reveal that the nanosheet morphology and crystallinity of the sample are degraded after the OER stability test **(Fig. S6 (a,b))**, and this is presumably due to gas evolution reactions on the surface.

4. Conclusions

In summary, we synthesized highly efficient $CuCo_2O_4$ nanosheets on a Ni foam substrate via an electrodeposition method as a bifunctional electrode for supercapacitor and electrochemical water splitting applications in alkaline KOH solutions. The $CuCo_2O_4$ nanosheet electrode exhibited a maximum specific capacitance of 1473 F/g at 1 A/g in a 3M KOH solution with an excellent capacity retention of 85% after 5000 cycles. The $CuCo_2O_4$ nanosheet electrode

also exhibited a superior OER activity with low overpotential of 260 mV at 20 mA/cm^2 and a Tafel slope of 64 mV/dec. The OER activity of the $CuCo_2O_4$ electrocatalyst was highly stable up to 25 h, confirming its chemical and structural durability in an extremely alkaline solution.

Acknowledgments

The authors would like to thank the financial support from the National Research Foundation (NRF) of Korea (Grant nos. 2015M2A2A6A02045251, 2018R1A2B6007436, 2016R1A6A1A03012877, and 2015R1D1A1A01060743).

References

1 C. Liu, F.Li, L.-P. Ma and H.-M. Cheng, *Adv. Mater.* 2010, **22**, E28.

2 A. L. M. Reddy, S. R. Gowda, M. M. Shaijumon and P. M. Ajayan, *Adv. Mater.* 2012, **24**, 5045.

3 J. Y.Hwang, M.F.El-Kady, Y.Wang, L.Wang, Y. Shao, K.Marsh, J. M. Ko and R. B. Kaner, *Nano Energy,* 2015, **18**, 57.

4 T. Audichon, T. W. Napporn, C. Canaff, C. Morais, C. Comminges and K. B. Kokoh, *J. Phys. Chem. C,* 2016, **120**, 2562.

5 V. Kannan, A. I. Inamdar, S. M. Pawar, H.-S. Kim, H.-C. Park, H. Kim, H.k Im and Y. S. Chae, *ACS Appl. Mater. Interfaces,* 2016, **8**, 17220.

6 H. Wang, H.-W. Lee, Y. Deng, Z. Lu, P.-C. Hsu, Y. Liu, D. Lin and Y. Cui, *Nature commun.,* 2015, **6**, 7261.

7 S. M. Pawar, J. Kim, A. I. Inamdar, H. Woo, Y. Jo, B.S. Pawar, S. Cho, H. Kim and H. Im, *Scientific Reports,* 2016, **6**,21310.

8 S. M. Pawar, B. S. Pawar, B. Hou, J. Kim, A. T. A. Ahmed, H. S. Chavan, Y. Jo, S. Cho, A. I. Inamdar, J. L. Gunjakar, H. Kim, SeungNam Cha and H. Im, *J. Mater. Chem. A,* 2017,**5**, 12747.

9 Y. Wang, T.Zhou, K. Jiang, P. Da, Z. Peng, J. Tang, B. Kong, W.-B. Cai, Z. Yang and G. Zheng, *Adv. Energy Mater.*, 2014, **4**, 1400696.

10 V.D. Nithya and N. S. Arul, *Journal of Power Sources,* 2016, **327**, 297.

11S. Haschke, Y.Wu, M. Bashouti, S. Christiansen and J.Bachmann, *ChemCatChem,* 2015, **7**, 2455.

12 M. Jana , S. Saha , P. Samanta, N. C. Murmu, N. H. Kim, T. Kuila and J. H. Lee , *Journal of*

Power Sources, 2017, **340**, 380.

13 W. Yuan, P. K. Shen and S. P. Jiang*, J. Mater. Chem. A,* 2014, **2**, 123.

14 K. K. Upadhyay, T. Nguyen, T. M. Silva, M. J. Carmezim and M. F Montemor, *Electrochimica Acta,* 2017, **225**, 19.

15 Y. Jin, H. Wang, J. Li, X. Yue, Y. Han, P.K. Shen and Y. Cui, *Adv. Mater.* 2016, **28**, 3785.

16 H. S. Jadhav, S.M. Pawar, A. H. Jadhav, G. M. Thorat and J.G. Seo, *Scientific Reports,* 2016, **6**, 31120.

17Y. Zhao, X. Zhou, Y. Ding , J. Huang, M. Zheng and W. Ye, *Journal of Catalysis,* 2016, **338**, 30.

18 S. Gao, X. Jiao, Z. Sun, W. Zhang, Y. Sun, C. Wang, Q. Hu, X. Zu, F. Yang and S. Yang, *Angew. Chem. Int.Ed*, 2016, **55**, 698.

19 F. Cheng, J. Shen, B. Peng, Y. Pan, Z. Tao and J. Chen, *Nat. Chem.*, 2011, **3**, 79.

20 S. Liu, K. San Hui, K. N. Hui, J. M. Yun and K. H. Kim, *J. Mater. Chem. A*, 2016, **4**, 8061.

21 B. Chi, H. Lin and J. Li*, Int. J. Hydrog. Energy*, 2008, **33**, 4763.

22 T. W. Kim, M. A. Woo, M. Regis and K.-S. Choi, *J. Phys. Chem. Lett.,* 2014, **5**, 2370.

23 S. Singh, P. Pramanik, S. Sangaraju, A. Mallick, L. Giebeler and S. Thota, *J. Appl. Phys.*, 2017, **121**, 194303.

24 Z.-Y. Yu, L.-F. Chen and S.-H. Yu, *J. Mater. Chem. A*, 2014, **2**, 10889.

25 M. Kuang, P. Han, Q. Wang, J. Li and G. Zheng, *Adv. Funct. Mater.*2016, **26**, 8555.

26 S. Liu, K.S. Hui and K.N. Hui, *ACS Appl. Mater. Interfaces,* 2016, **8**, 3258.

27K. K. Naik, S. Sahoo and C. S. Rout, *Microporous and Mesoporous Materials,* 2017, **244**, 226.

28 S. K. Bikkarolla and P.Papakonstantinou, *Journal of Power Sources,* 2015, **281**, 243.

29 Y. Wang, D. Yang, J. Lian, J. Pan, T. Wei and Y. Sun, *Journal of Alloys and Compounds,* 2018,**735**, 2046.

30 S. Liu, D. Ni, H.-F. Li, K. N.Hui, C.-Y. Ouyang and S. C. Jun, *J. Mater. Chem. A,* 2018,**6**, 10674.

31 A.T. A. Ahmed, B. Hou, H. S. Chavan, Y. Jo, S. Cho, J. Kim, S. M. Pawar, S. Cha, A. I. Inamdar, H. Kim and H. Im , *Small* , 2018, 1800742.

32 L. Abbasi and M. Arvand, *Applied Surface Science*, 2018,**445**,272.

33 H. Chen, X. Chen, Y. Zeng, S. Chen and J. Wang, *RSC Adv*., 2015,**5**,70494.

34 J. Cheng, H. Yan, Y. Lu, K. Qiu, X. Hou, J. Xu, L. Han, X. Liu, J.-K. Kim and Y. Luo, *J. Mater. Chem. A,* 2015,**3**, 9769.

35 S. Vijaykumar, S.-H. Lee and K.-S. Ryu, *Electrochimica Acta*, 2015, **182**,979.

36 L. Liao, H. Zhang, W. Li, X. Huang, Z. Xiao, K. Xu, J. Yang, R. Zou and J.Hu, *J. Alloys Compd.,* 2017, 695,3503.

37 A. Pendashteh, M. S. Rahmanifar, R. B. Kanerc and M. F. Mousavi, *Chem. Commun.*, 2014, **50**, 1972.

38 A. Pendashteh, S. E. Moosavifard, M. S. Rahmanifar, Y. Wang, M. F. El-Kady, R. B. Kaner and M. F. Mousavi, *Chem. Mater.*, 2015, **27**, 3919.

39. S. K. Kaverlavani, S. E. Moosavifard and A. Bakouei, *Chem. Commun.,* 2017, **53**, 1052.

40 B. Mendoza-Sánchez and Y. Gogotsi, *Adv. Mater*. 2016, **28**, 6104.

41 X. Du, X. Zhang, Z. Xu, Z. Yang and Y. Gong, *Int. J. of hydrogen energy,2018,* **4 3**, 5 0 1 2.

42 G. Wei, J. He, W. Zhang, X. Zhao, S. Qiu and C. An, *Inorg. Chem.* 2018, **57**, 7380.

43 A. Karmakar, S. K. Srivastava, *ACS Appl. Mater. Interfaces,* 2017, **9**, 22378.

44 Y. S. Park, C. S. Park, C. H. Kim and Y. D. Kim, *Journal of the Korean Physical Society*, 2016, **69**, 1187.

45 X. Lu and C. Zhao, *Nature Commun.*2015,**6**,6616.

46 Y. Yang, K. Zhang, H. Lin, X. Li, H. C. Chan, L. Yang and Q. Gao, *ACS Catal*. 2017, **7**, 2357.

47 J. Kim, C. Park , S. M. Pawar,A. I. Inamdar, Y. Jo, J. .Han, J. P. Hong , Y. S. Park, D. -Y.

Kim, W. Jung, H. Kim and H. Im, *Thin Solid Films,* 2014, **566**, 88.

48 W. Song, Z. Ren, S.-Y. Chen, Y. Meng, S. Biswas, P. Nandi, H. A Elsen, P.-X. Gao and S. L. Sui, *ACS Appl. Mater. Interfaces,* 2016, **8**, 20802.

49 X. Pan, X. Chen, Y. Li and Z. Yu, *Electrochimica Acta,* 2015, **182**,1101.

50 C. Yuan, L. Yang, L. Hou, L. Shen, X. Zhang and X. W. Lou, *Energy Environ. Sci.* 2012, **5**, 7883.

51 B. Hou, D. Parker, G. P. Kissling, J. A. Jones, D. Cherns and D. J. Fermín, *J. Phys. Chem. C* 2013, **117** , 6814.

52 J. L. Gautier, E. Trollund, E. Rios, P. Nkeng and G. Poillerat, *J. Electroanal. Chem.*, 1997, **428**, 47.

53 S. Liu, R. Zhang, W. Lv, F. Kong and W. Wang, *Int. J. Electrochem. Sci*., 2018**, 13**, 3843.

54 A. D. Jagadale, V.S. Kumbhar, R. N. Bulakhe and C.D. Lokhande, *Energy,* 2014, **64**, 234.

55 S. K. Kaverlavani, S. E. Moosavifard and A. Bakouei, *J. Mater. Chem. A*, 2017, **5**, 14301.

56 A. Sivananthan,P.Ganesan and S.Shanmugam, *Adv.Funct. Mater.*, 2016, **26**, 4661.

57 J.Yu,C.Lv,L.Zhao,L.Zhang,Z.Wang and Q.Liu, *Adv.Mater.Interfaces*, 2018, **5**, 1701396.

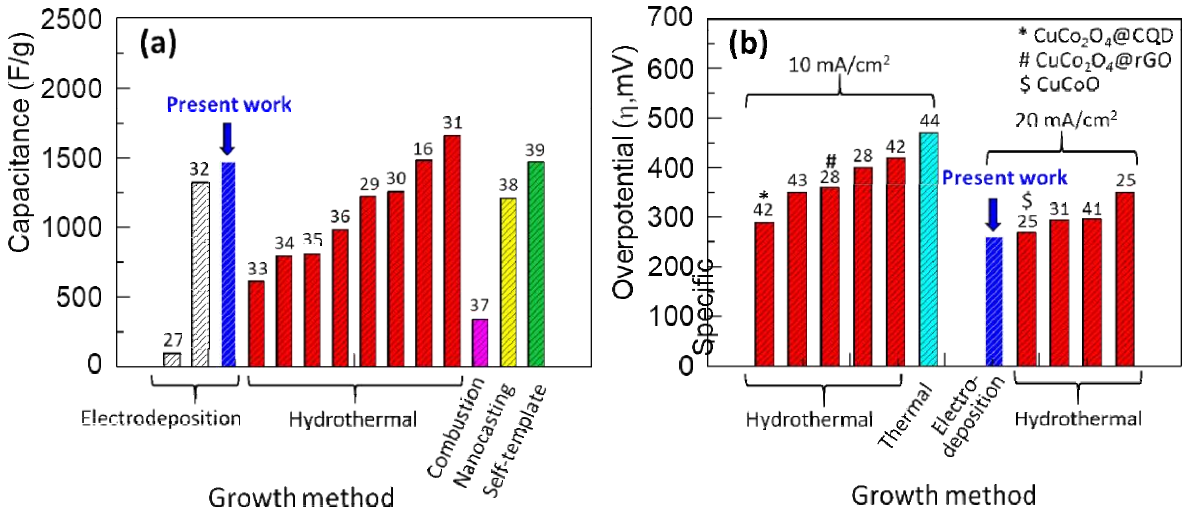

Figure 1: Comparative representation of the electrochemical performances, i.e. supercapacitor and oxygen evolution reaction (OER) properties of $CuCo_2O_4$ based materials.

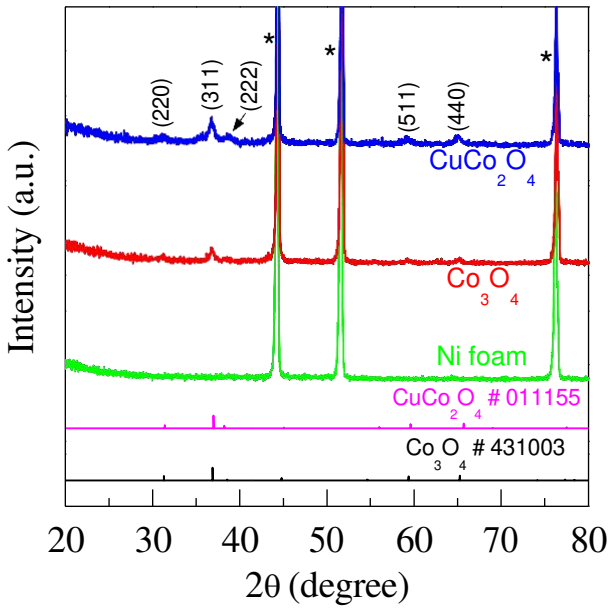

Figure 2: X-ray diffraction pattern of the Co_3O_4 and $CuCo_2O_4$ nanosheet films.

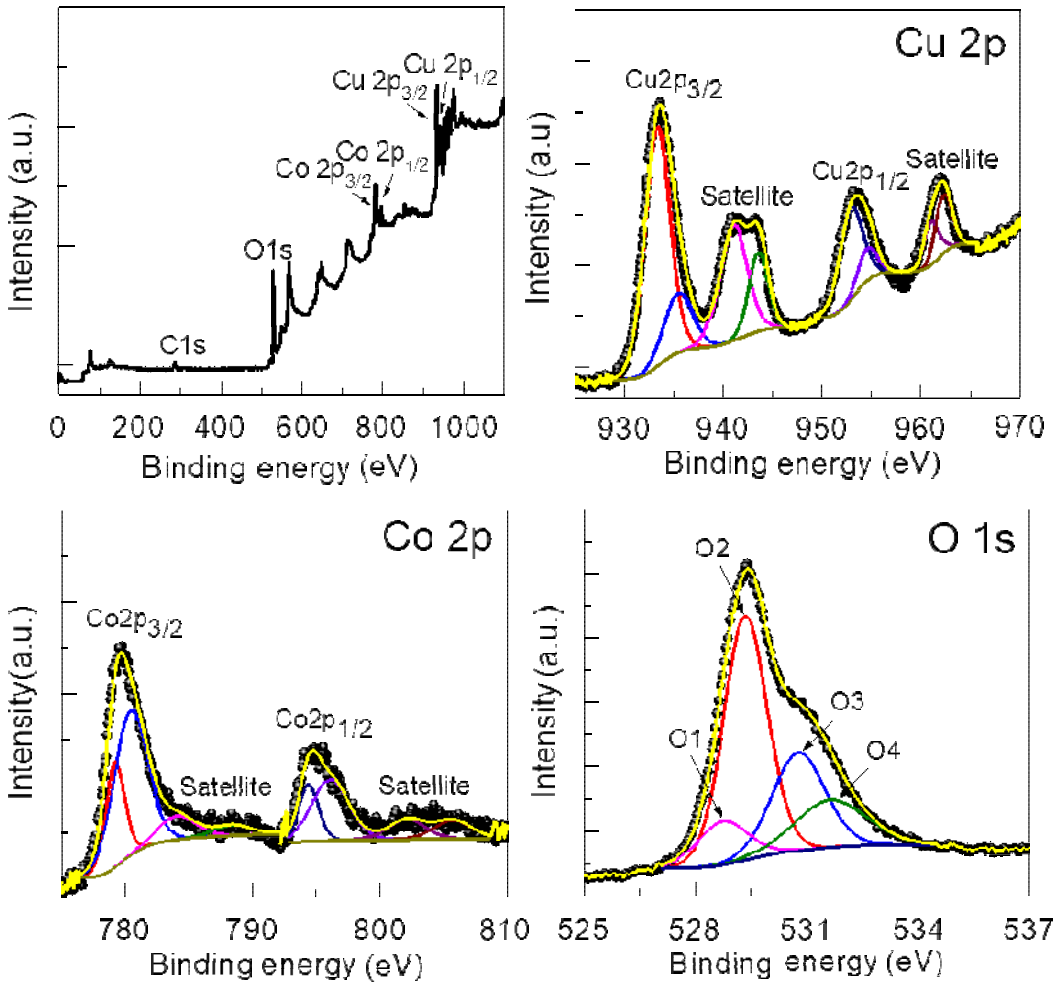

Figure 3: Survey spectrum and deconvoluted peaks of Cu 2p, Co 2p and O1s of the $CuCo_2O_4$ nanosheet thin film.

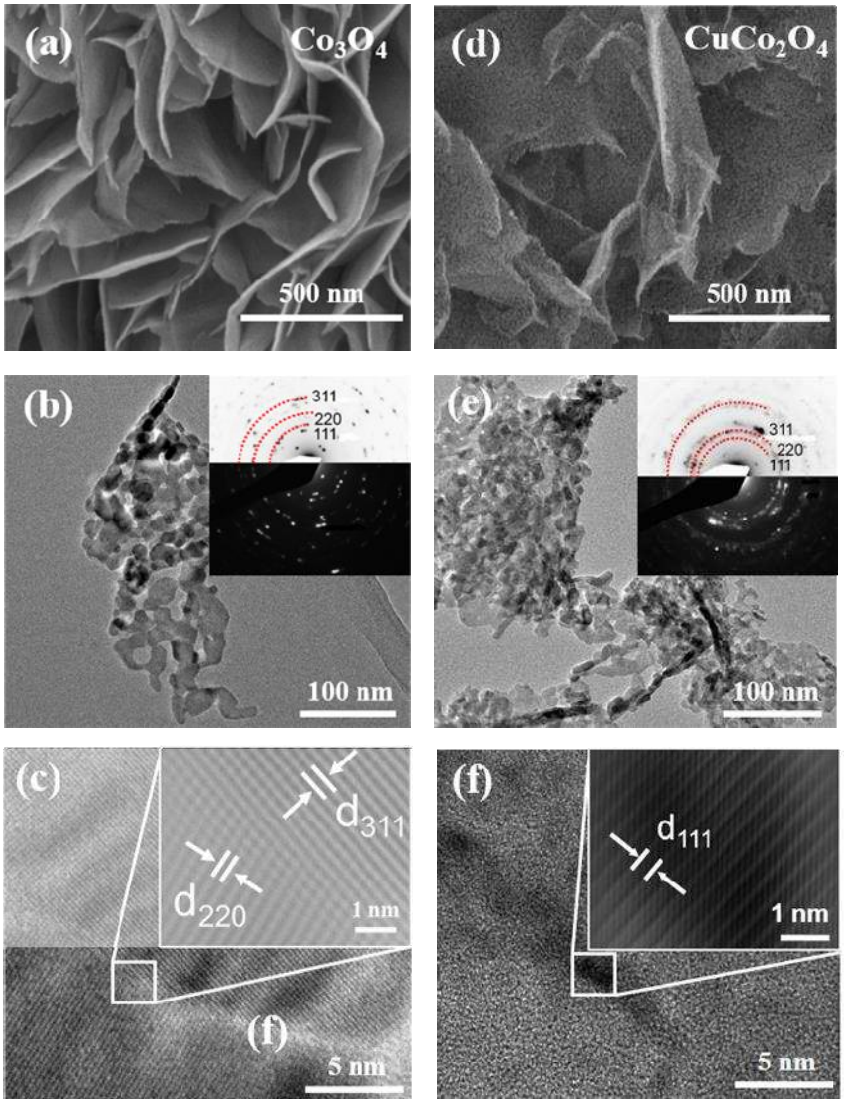

Figure 4: FE-SEM images of the (a) Co_3O_4 and (d) $CuCo_2O_4$ nanosheet films. (b) TEM and (c) HR-TEM images of the Co3O4 nanosheet film. (e) TEM and (f) HR-TEM images of the $CuCo_2O_4$ nanosheet film. The insets in (b) and (e) show SAED patterns. The insets in (c) and (f) show the magnified images of a selected area of the HR-TEM images with a scale bar of 1 nm.

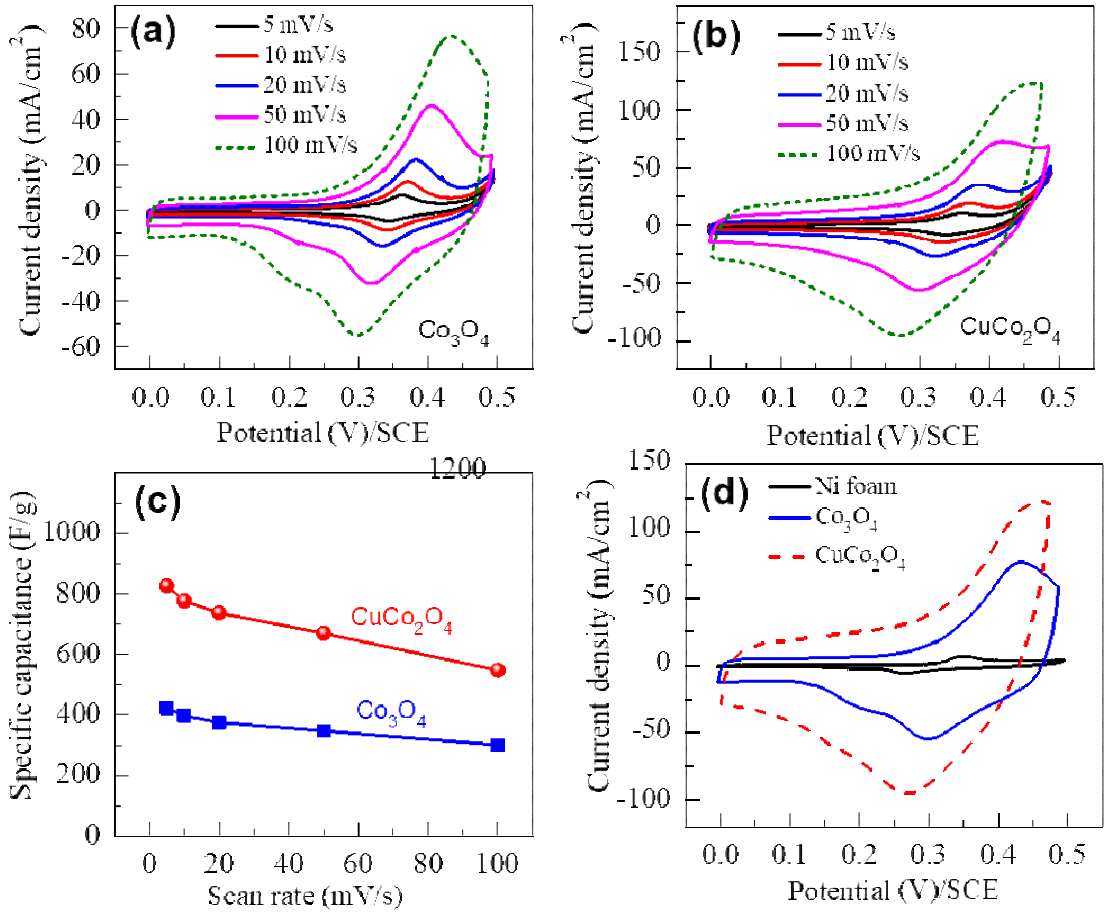

Figure 5: Cyclic voltammogram (CV) curves at different scan rates for (a) Co_3O_4 and (b) $CuCo_2O_4$. (c) Specific capacitance versus scan rate. (d) Comparative CV curves of Ni foam, Co_3O_4 and $CuCo_2O_4$ nanosheet electrodes at 100 mV/s.

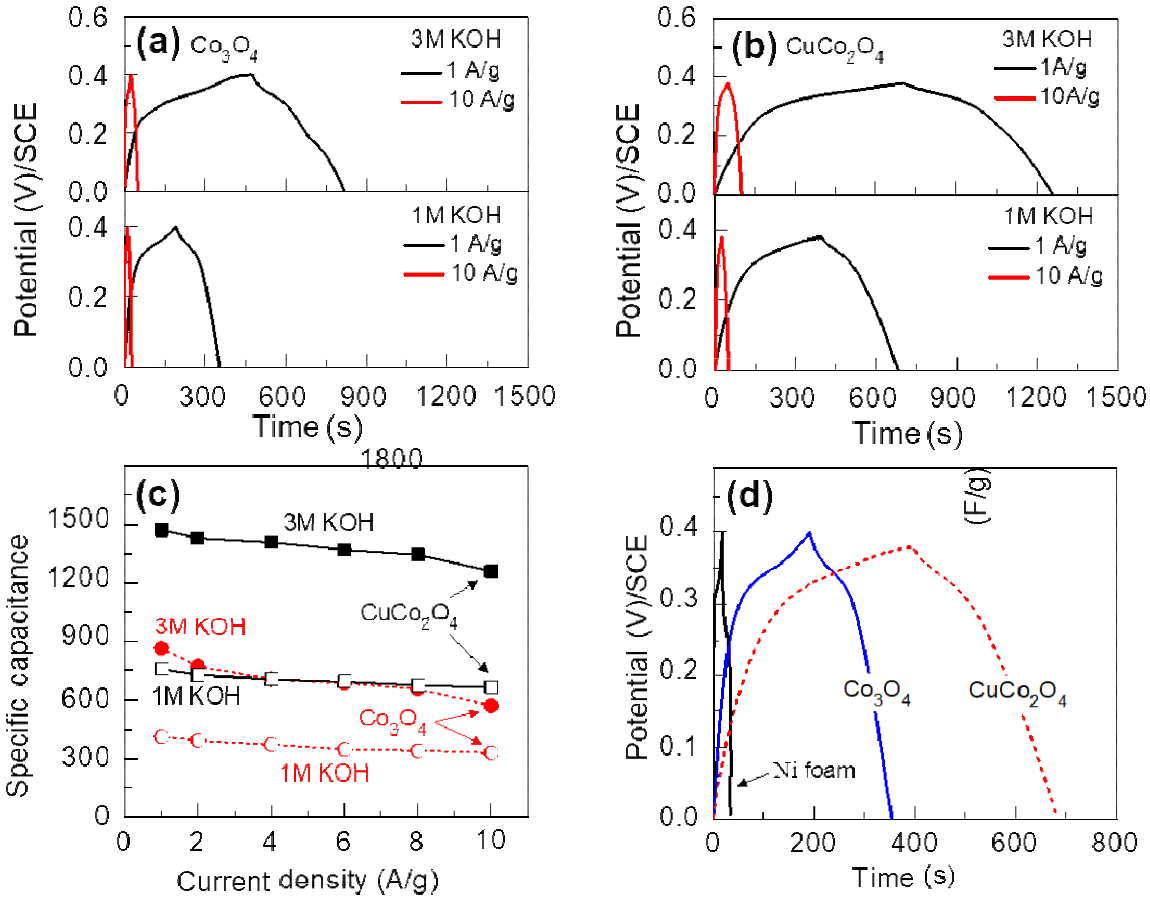

Figure 6: Galvanostatic charge-discharge (GCD) curves of (a) Co_3O_4 and (b) $CuCo_2O_4$. (c) Specific capacitance versus current density. (d) Comparative GCD curves of Ni foam,Co_3O_4 and $CuCo_2O_4$ nanosheet electrodes at 1 A/g in 1M KOH.

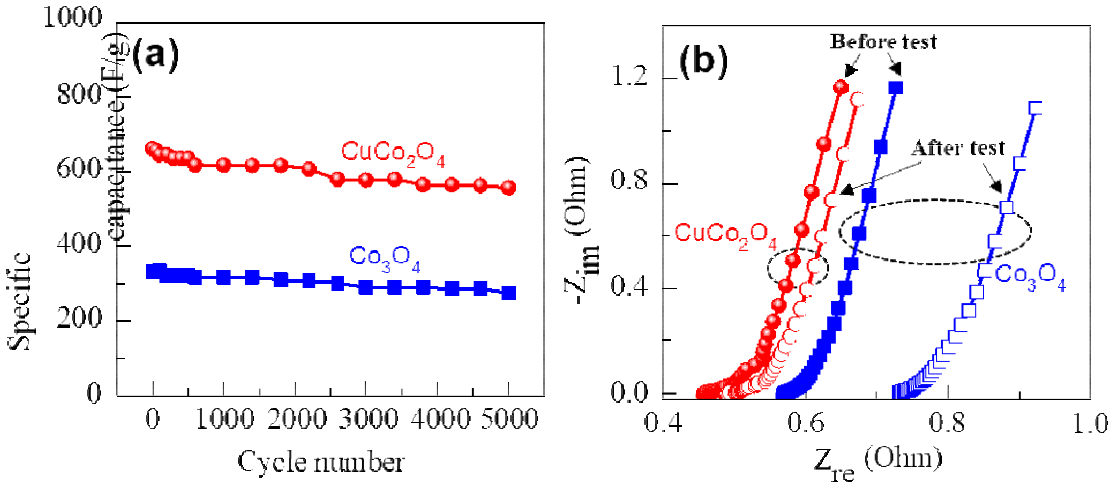

Figure 7: Long term cyclic stability of Co_3O_4 and $CuCo_2O_4$ nanosheet electrodes, and (b) EIS spectra of Co_3O_4 and $CuCo_2O_4$ nanosheet electrodes before and after the stability test.

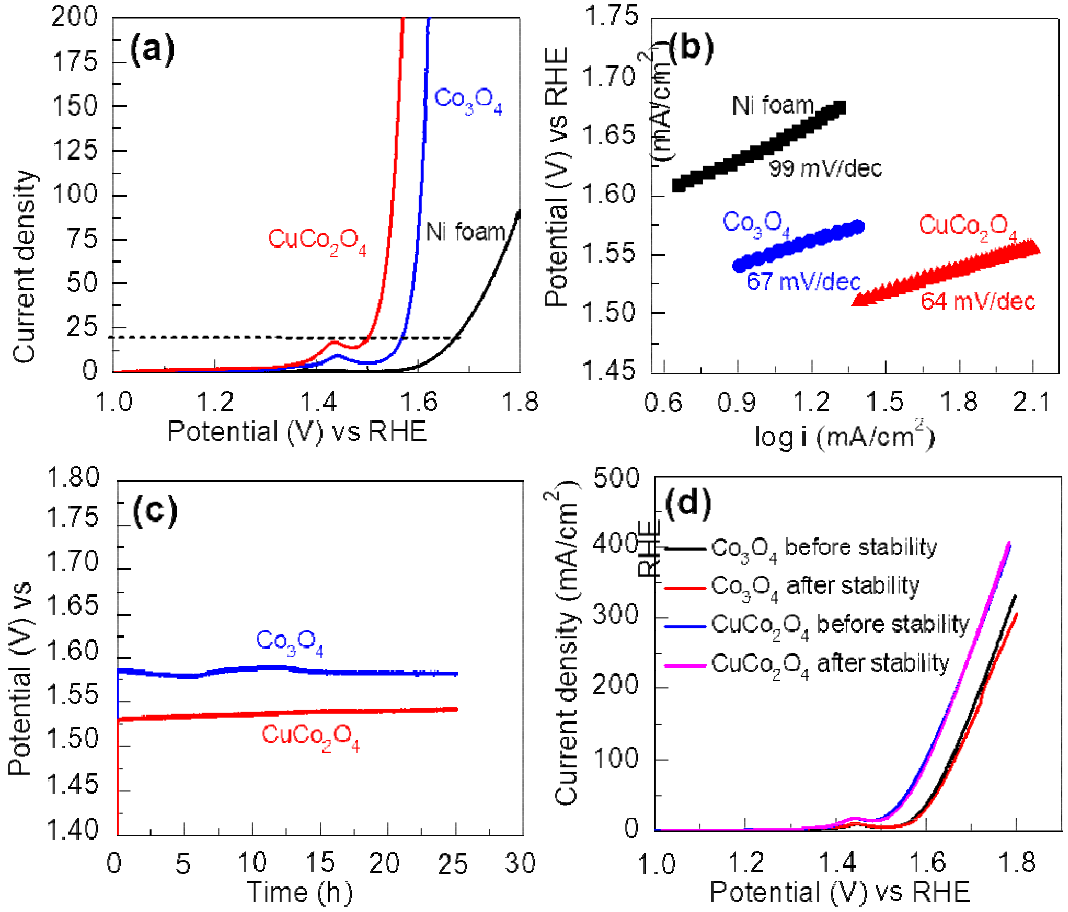

Figure 8: (a) OER LSV polarization curves (iR corrected) of Co_3O_4 and $CuCo_2O_4$ nanosheet electrodes at a scan rate of 5 mV/s, and (b) the corresponding OER Tafel plot, (c) Chronopotentiometry stability test measured at 20 mA/cm^2 for 25 hours, and (d) LSV curves of Co_3O_4 and $CuCo_2O_4$ nanosheet electrodes before and after the stability test.

Supplementary information for

Nanoporous CuCo2O4 nanosheets as a highly efficient bifunctional electrode for supercapacitors and water oxidation catalysis

S. M. Pawar,[a] B. S. Pawar,[a] P. T. Babar,[b] ATA Ahmed,[a] H.S. Chavan,[a] Yongcheol Jo,[a] Sangeun Cho,[a] Jongmin Kim,[a] B. Hou,[c] A. I. Inamdar,[a] SeungNam Cha,[c] Jin Hyeok Kim,[b] Hyungsang Kim [a] and Hyunsik Im [a]

[a] Division of Physics and Semiconductor Science, Dongguk University, Seoul 04620, South Korea

[b] Optoelectronic Convergence Research Center, Department of Materials Science and Engineering, Chonnam National University, Gwangju 500-757, South Korea

[c] Department of Engineering Science, University of Oxford, Parks Road, OX1 3PJ, UK

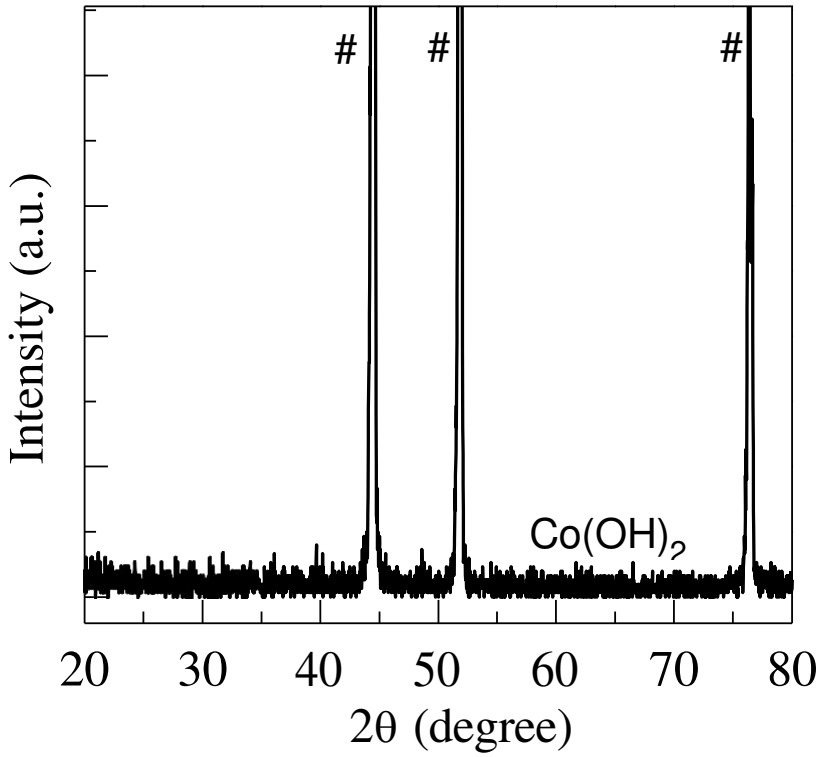

Fig. S1. XRD pattern of the as-deposited $Co(OH)_2$ nanosheet film.

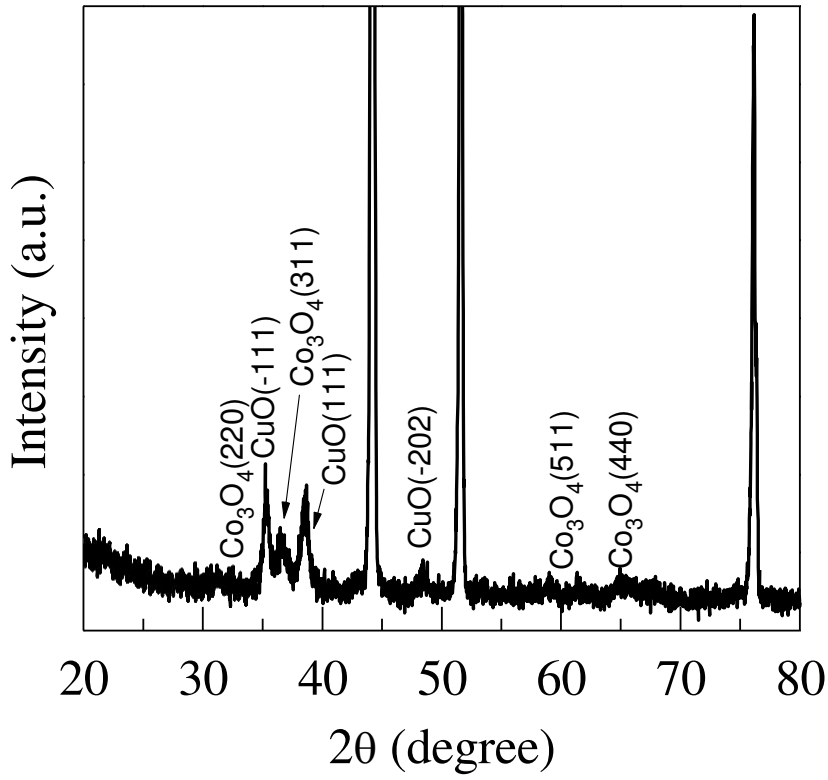

Fig. S2. XRD pattern of the Cu-Co oxide nanosheet film deposited using a 5 mM $Cu(NO_3)_2$ solution. Two different phases, CuO and Co_3O_4, are detected.

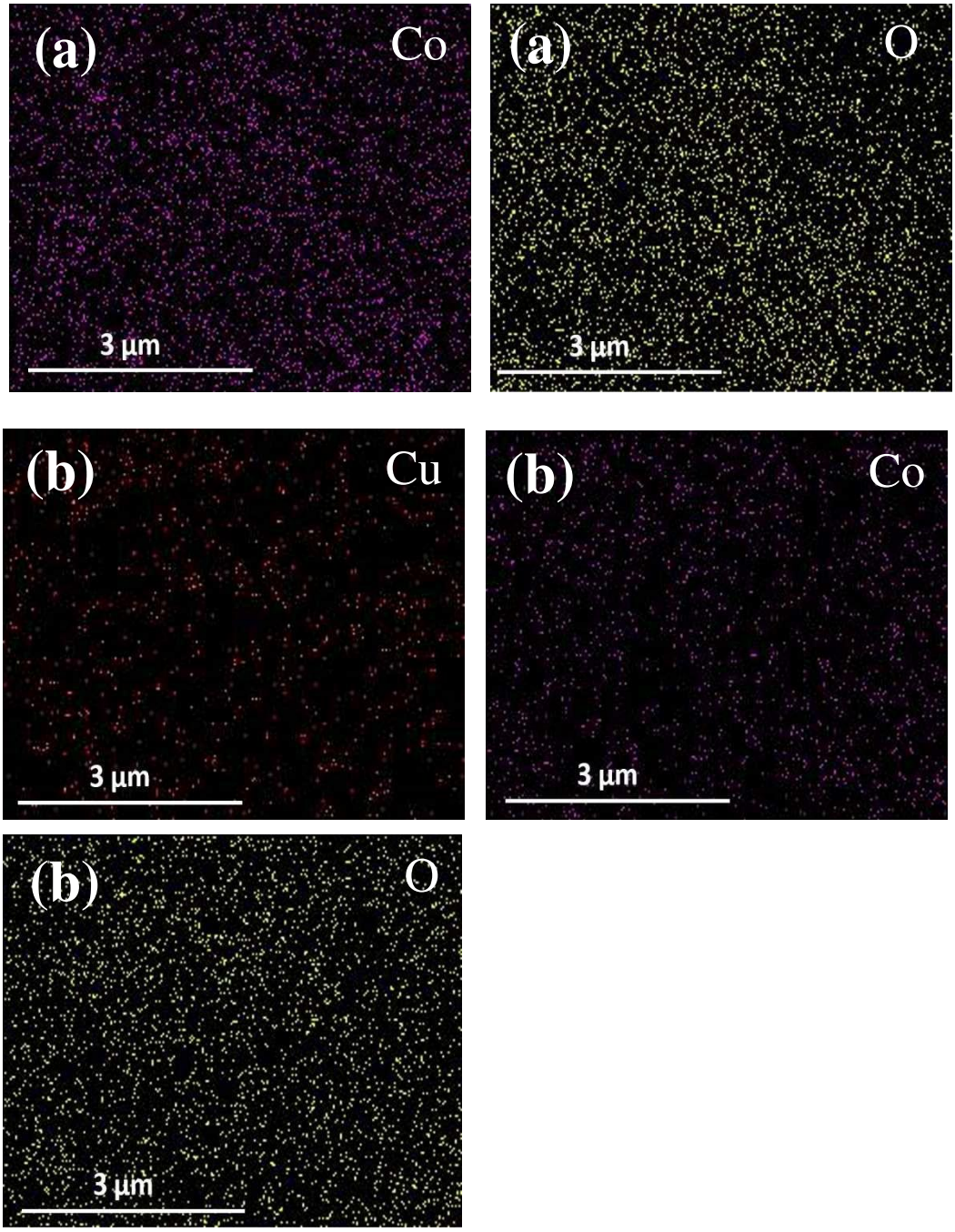

Fig. S3. EDS elemental mapping of (a) Co_3O_4 and (b) $CuCo_2O_4$ nanosheet thin films.

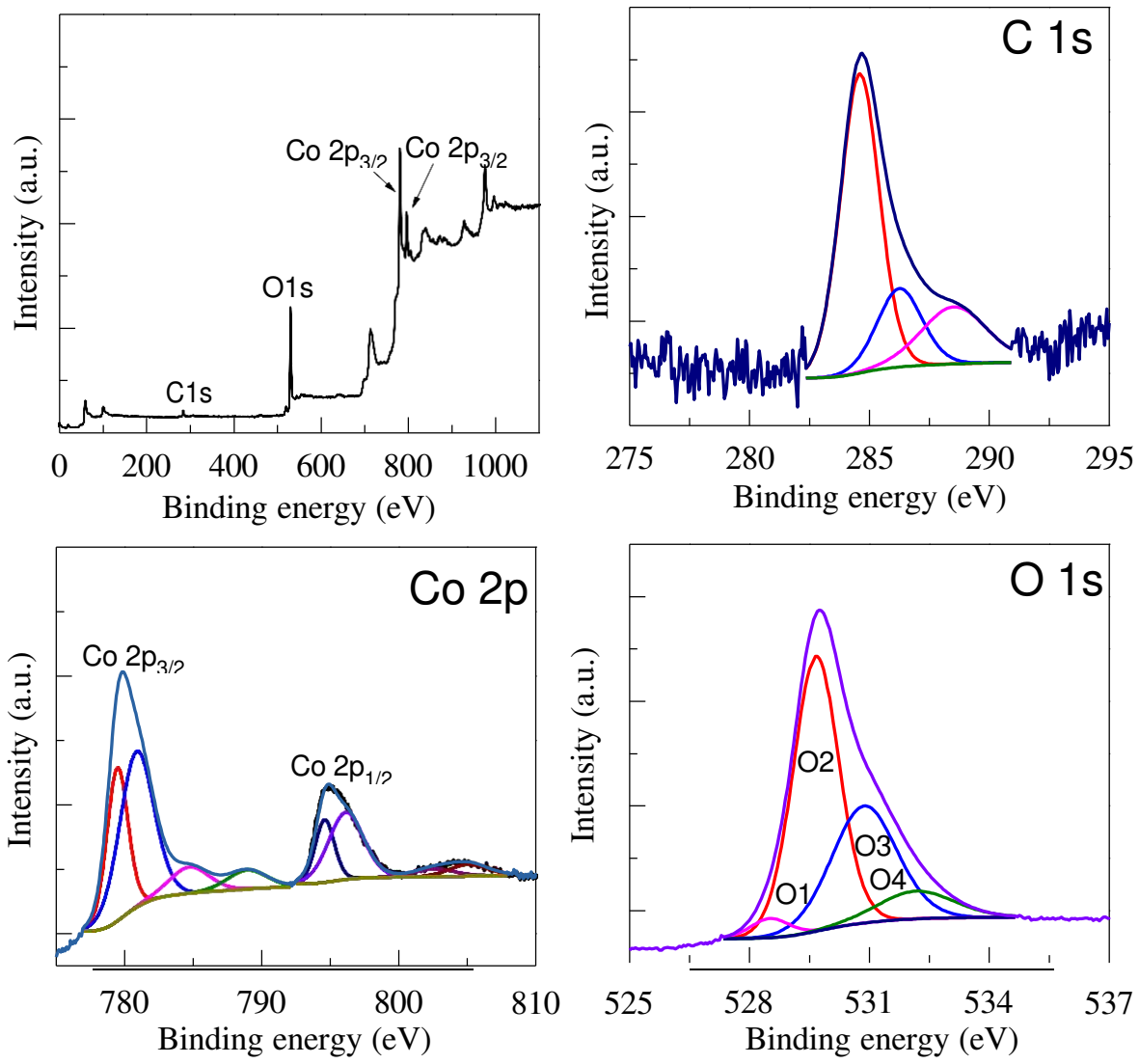

Fig. S4. XPS survey spectrum and deconvoluted peaks of (a) C 1s, (b) Co 2p, and (c) O 1s for the Co_3O_4 nanosheet thin film.

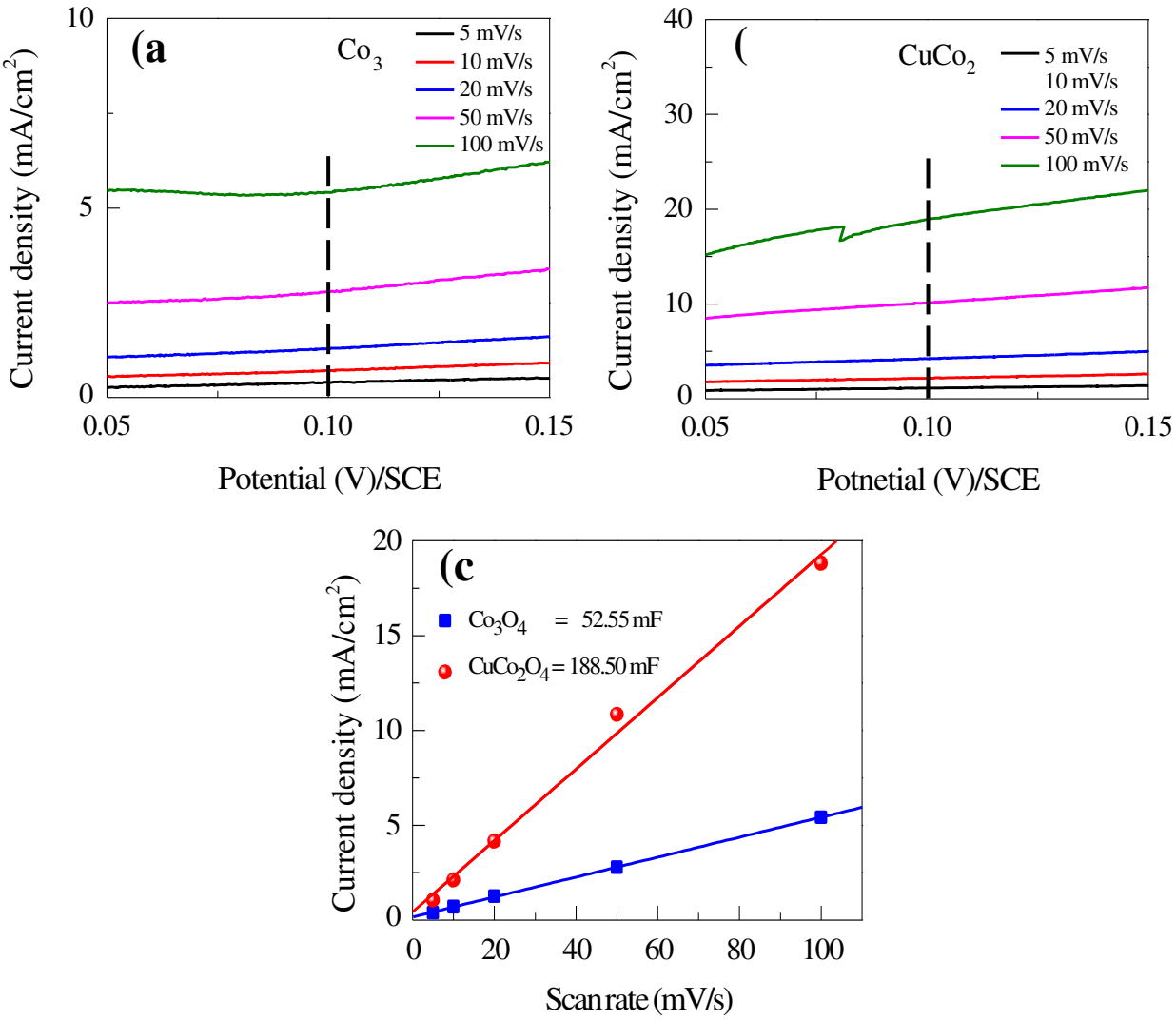

Fig. S5. (a,b) Linear charging region of the CV curves of the Co_3O_4 and $CuCo_2O_4$ electrodes, and **(c)** i_{DL} versus v curves of the electrodes measured at 0.1 V.

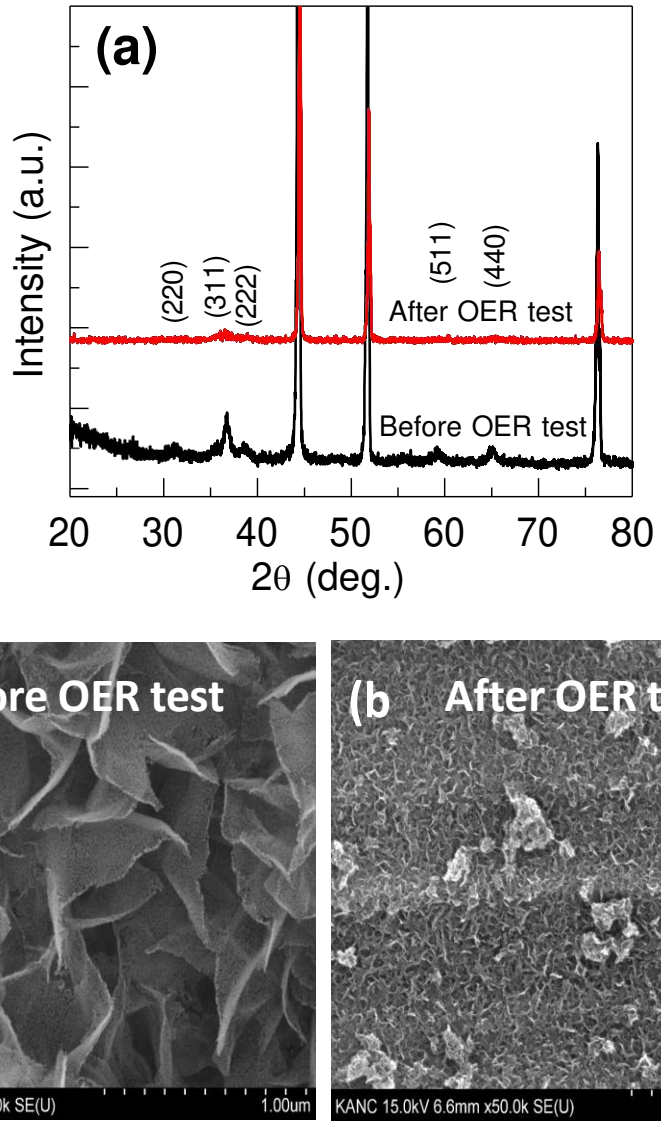

Fig. S6: (a) X-ray diffraction patterns and (b) SEM images of the $CuCo_2O_4$ nanosheet electrode before and after the OER test.

Table S1. Compositional analysis of the Co_3O_4 and $CuCo_2O_4$ nanosheets.

	Cu	**Co**	**O**
Co_3O_4		36.15	63.85
$CuCo_2O_4$	14.48	29.49	56.03

Table S2. Electrochemical supercapacitor performances of $CuCo_2O_4$ based materials.

Material	Synthesis method	Electrolyte conc.	Specific capacitance	Cycles	Capacity retention	Ref.
$CuCo_2O_4$ nanosheet	Electrodeposition	6 M KOH	100 F/g @ 1A/g	3000	175 % @ 10 A/g	[27]
$CuCo_2O_4$ nanosheets	Electrodeposition	3M KOH	1330 F/ g @ 2 A g^{-1}	5000	93.6 % @ 10 A/g	[32]
$CuCo_2O_4$ Nanoporous sheet	Electrodeposition	1M KOH	760 F/g @ 1 A/g	5000	85 % @ 10 A/g	Present work
		3M KOH	1473 F/g @ 1 A/g	-	-	
$CuCo_2O_4$ nanowires	Hydrothermal	2M KOH	611 F/g@ 1.7 A/g	8000	94.8 %@ 10 mA/cm^2	[33]
$CuCo_2O_4$ nanograss	Hydrothermal	2 M KOH	796 F/g@ 2 A/g	5000	94.7 % @ 2 A/g	[34]
$CuCo_2O_4$ nanobelts	Hydrothermal	2M KOH	809 F/ g@ 0.66 A/ g	1800	127 % @ 10.6 A/g	[35]
$CuCo_2O_4$ nanowires	Hydrothermal	3M KOH	982 F/g @ 1.5 A/g	3000	100.94 % @ 50mV/s [36]	
cedar leaf-like $CuCo_2O_4$	Hydrothermal	2M KOH	1223 @ 1.08 A/g	2000	88 % @ 10.81 A/g	[29]
$CuCo_2O_4$ nanowire	Hydrothermal	1 M KOH	1256 F/g @ 1 A/g	5000	85.2 @ 10 A/g	[30]
$CuCo_2O_4$ Nanoflower	Hydrothermal	2 M KOH	1480 F/g @ 2A/g	3000	129 % @ 100 mV/s	[16]
$CuCo_2O_4$ nanosheet	Hydrothermal	2M KOH	1658 F/g @ 1 A/g	5000	90 % @ 20 A/g	[31]
$CuCo_2O_4$ nanostructure	Combustion method	3M KOH	338 F/g @ 1 A/ g	4000	86 % @ 10 A/g	[37]
$CuCo_2O_4$ nanowire	Nanocasting from silica template	6 M KOH	1210 F/g@ 2A/g	4000	93.5 % @ 20 A/g	[38]
CuCo2O4 Microsphere	Self-template	3M KOH	1472 F/g@ 2A/g	5000	93.8 % @ 10 mA/cm^2	[39]

Table S3. Comparison of OER activity of $CuCo_2O_4$ based electrocatalysts in alkaline media.

Catalyst	Synthesis method	Electrolyte	Onset overpotential (mV)	Tafel slope (mV/dec)	Overpotential (η) @ 10 mA/cm^2	Ref.
$CuCo_2O_4$ nanosheet	Electrodeposition	1M KOH	240	64	260@ 20 mA/cm^2	Present work
CuCoO nanowire	Hydrothermal	1M KOH	250	68	270@ 20 mA/cm^2	[25]
$CuCo_2O_4$ Nanowire		1M KOH	290	75	350 @ 20 mAcm^2	
$CuCo_2O_4$ nanosheet	Hydrothermal	1M KOH	-	117	294 @ 20 mA/cm^2	[31]
$CuCo_2O_4$ microflower	Hydrothermal	1M KOH	-	50	296@ 20 mA/cm^2	[41]
$CuCo_2O_4$ polyhedron	Hydrothermal	1M KOH	330	90.3	420	[42]
$CuCo_2O_4$@ CQD nanowires	Hydrothermal	1M KOH	230	64	290	
$CuCo_2O_4$ nanochain	Hydrothermal	1M KOH	270	63.3	351	[43]
$CuCo_2O_4$ nanoparticle	Hydrothermal	1M KOH	-	67	400	[28]
$CuCo_2O_4$/ rGo nanoparticle			-	64	360	
$CuCo_2O_4$ nanopowder	Thermal decomposition	1M KOH	-	-	470	[44]